J. Fluid Mech. (2007), *vol.* 574, *pp.* 1–23.
doi:10.1017/S0022112006003879 Printed in the United Kingdom

Scaling and instability of a junction vortex

J. J. ALLEN[1] AND T. NAITOH[2]

[1]Department of Mechanical Engineering, New Mexico State University, Las Cruces, NM 88003, USA

[2]Department of Systems Engineering, Nagoya Institute of Technology, Gokiso-cho, Showa-ku, Nagoya 446, Japan

(Received 9 May 2006 and in revised form 7 August 2006)

This paper details experiments in the region where an impulsively started moving wall slides under a stationary wall. The experiments were conducted over a Reynolds number range of $Re_\Gamma = 5 \times 10^2$–$5 \times 10^5$. The length scale for the Reynolds number is defined as the distance the wall has moved from rest and increases during an experiment. Experiments show that for $Re_\Gamma > 10^3$ a vortex forms close to the junction where the moving wall meets the stationary one. The data shows that while the vortical structure is small, in relation to the fixed-apparatus length scale, the size of the vortex normalized with respect to the wall speed and viscosity scales in a universal fashion with respect to Re_Γ. The scaling rate is proportional to $t^{5/6}$ when the Reynolds number is large. The kinematic behaviour of the vortex is related to the impulse that the moving wall applies to the fluid and results in a prediction that the transient structure should grow as $t^{5/6}$ and the velocity field should scale as $t^{-1/6}$. The spatial-growth prediction is in good agreement with the experimental results and the velocity scaling is moderately successful in collapsing the experimental data.

For $Re_\Gamma > 2 \times 10^4$ three-dimensional instabilities appear on the perimeter of the vortical structure and the flow transitions from an unsteady two-dimensional flow to a strongly three-dimensional vortical structure at $Re_\Gamma \simeq 4 \times 10^4$. The instability mechanism is centrifugal. The formation and growth of these instability structures and their ingestion into the primary vortex core causes the three-dimensional breakdown of the primary vortex. Two movies are available with the online version of the paper.

1. Introduction

1.1. *Background*

When an impulsively started moving wall slides under a stationary wall the potential exists for a vortical structure to develop close to their junction. The formation mechanism for this vortex is that when the wall is set into motion a Stokes layer develops over the moving surface and this layer is driven, by shear forces, past the singularity at the junction and over the stationary wall. Vorticity of opposite sign then develops over the stationary wall to enforce the no-slip condition. The flow field over the stationary wall initially resembles an unsteady wall jet. If the Reynolds number $Re_\Gamma = U_w L/\nu$, where L is the distance that the wall has moved from rest and U_w is the wall speed, is large enough then the jet separates and rolls into a vortex. A schematic of the development process is shown in figure 1(*a*).

This type of vortical structure is generated in a range of industrial situations, the most important being at the head of a piston as it moves through a cylinder; see Obokata & Okajima (1992) and Guezet & Kageyama (1997). Experimental studies

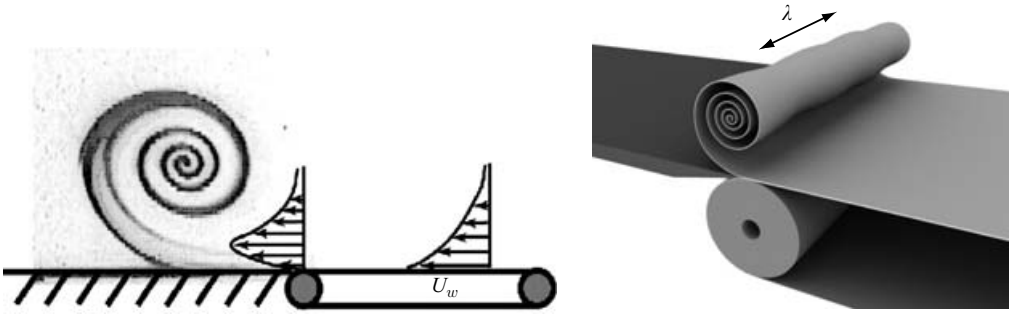

FIGURE 1. (*a*) A two-dimensional schematic of vortex development at the junction of a moving and a stationary surface and (*b*) the appearance of a three-dimensional spanwise instability wave. See also figure 2.

examining the development of this structure have typically consisted of an apparatus that uses a piston moving through a cylinder. This results in the formation of a vortex ring (or piston vortex) in front of the piston. Historically the use of a piston–cylinder geometry was motivated by the desire to analyse the flow inside an internal combustion engine. Hughes & Gerrard (1971) studied piston-vortex development for low Reynolds number, $2 \times 10^2 < Re_\Gamma < 4 \times 10^3$. They suggested a minimum Reynolds number for vortex formation of $Re_D = 200$, where the length scale in Re_D is the piston diameter. In terms of Re_Γ the data of Hughes & Gerrard (1971) would suggest that for $Re_\Gamma \simeq 1$–500 a vortex forms.

Tabaczynski, Hoult & Keck (1970) conducted experiments examining the development of the piston vortex for high Reynolds number, $Re_\Gamma = 10^3$–10^5. The piston vortex was present in all their visualizations and they identified the transition of the vortex from a laminar to a turbulent structure at $Re_\Gamma \simeq 1.5 \times 10^4$. Self-similar relationships were proposed for the spatial growth of the 'area' of the vortex in the laminar and turbulent regimes. These relationships applied when the size of the vortex ring was small in relation to the piston diameter. The experiments of Allen & Chong (2000) measured the developing vorticity field of the piston vortex for the Reynolds number range $5 \times 10^2 < Re_\Gamma < 3 \times 10^4$. It was found that the strength of the piston vortex was about 25% of the strength of the circulation swept into the corner region by the moving wall. This indicates that significant vorticity cancellation was occurring with the opposite-sign vorticity that develops on the piston face.

An analytic solution for the steady viscous flow field in the junction region was developed by Taylor (1960). This solution is often referred to as the 'scraping-corner solution'. Taylor's solution geometry consisted of a scraper orientated at 90 degrees to the moving wall. However, it is trivial to modify the solution so that the scraper is in-plane with the moving wall, and the salient features of the solution remain: regions of opposite-sign vorticity in the corner-junction region. The region of validity of this viscous similarity solution is $rU_w/\nu \ll 1$, where r is the radial distance from the corner junction. At the junction of the moving and stationary surfaces the solution is singular in the pressure and the vorticity. The singularity is physically relieved by the presence of a small gap between the moving surfaces. Hancock, Lewis & Moffatt (1981) extended this steady solution to include inertial effects. The range of validity of the inertial expansion is $rU_w/\nu \simeq 5$. Again this solution can be simply modified so that the scraper is in-plane with the moving wall and the salient features of the solution

remain unchanged. The velocity profile over the stationary plate, with the inertial correction, appears similar to that of a wall jet. Wall jets consist of an inner layer that resembles a wall boundary layer and an outer layer that resembles a free shear layer. Both these layers are unstable at sufficiently high Reynolds number. Bajura & Catalano (1975) studied the instability and lift-off of the wall jet and suggested that they were the result of a phase dislocation of the instability structures in the inner and outer layers. In their experiments the streamwise location where lift-off occurred was an order of magnitude greater than the size of the separating structure, i.e. the jet was able to travel a considerable distance before separation occurred. However, as separation in the impulsively started experiments of Tabaczynski *et al.* (1970) and Allen & Chong (2000) occurred almost immediately, it was not a result of the 'lift-off' mechanism described above. Conlon & Lichter (1995) studied the transient start-up of a wall jet in order to clarify the behaviour of the head of the jet. The transient flow was characterized by the formation of either a dipole or a monopole at the head of the jet. They established that the relative strengths of the vorticity distribution in the outer and inner regions of the wall jet were important in determining whether a dipole or monopole formed during the start-up process. The features of their simulations, the roll-up of the outer-layer vorticity into a coherent structure and the stretching of the secondary vorticity, the near-wall layer, around the periphery of the primary vortex have a strong resemblance to the experimental work of Allen & Chong (2000). Conlon & Lichter (1995) noted that linear stability methods were not relevant to the description of the transient problem and that the initial formation of the rotational structure may be related to the instability that forms on a vorticity front as it enters a region of irrotational flow; see Stern & Pratt (1985). Conlon & Lichter (1995) commented that at low Reynolds numbers viscous diffusion acts quickly enough to prevent either monopole or dipole formation.

A full description of the transient requires an understanding of the transition of the flow field from a viscous flow to a flow dominated by inertial effects. The behaviour of viscous starting jets was considered by Cantwell (1986), who calculated the evolving topology of the flow field resulting from the application of a time-varying point force to an infinite fluid domain. In the absence of external length scales he was able to calculate the self-similar topology of the flow field and relate its evolution to the non-dimensional impulse (or Reynolds number Re_I) applied to the flow. Two critical Reynolds numbers were calculated that represent the transition between three distinct flow topologies. In order to interpret these bifurcations he calculated the entrainment diagram for the jet, based on particle-path equations. At low Re_I the topology of the leading front of the starting jet did not possess a rotating head; see diagram 1 in figure 2(*c*) of Cantwell (1986). The particle paths appear to converge toward a single node located on the horizontal axis. At $Re_I \simeq 1.2$ a bifurcation occurred from the single node to an on-axis saddle and off-axis nodes; see diagram 2; in figure 2(*c*) of Cantwell (1986). As the Reynolds number was further increased, to $Re_I \simeq 2.2$, a second transition occurred that resulted in the transformation of the nodes into foci; see diagram 3 in figure 2(*c*) of Cantwell (1986). It is the second bifuraction that represents the initiation of the characteristic vortex roll-up associated with the head of a starting jet. Cantwell's paper has important implications for the current study as it suggests a transition pathway, from an impulsively started non-rotating viscous jet into a jet with a leading vortical structure. Although the vortex of the current study is not generated by a point force, there are many features in common with Cantwell's study, such as the absence of an external-apparatus length scale and the dependence of the transition on a developing Reynolds number.

1.2. *Instability development*

The experiments of Tabaczynski *et al.* (1970) document the transition of the piston vortex from a laminar to a turbulent structure. Although the mechanism for transition was not discussed, the rate of growth of the turbulent structure was more rapid than that of the laminar structure. This was due to entrainment by the three-dimensional instabilities that appear on the periphery of the structure, which is similar to the growth mechanism of a turbulent vortex ring; see Glezer & Coles (1990). The experiments of Allen & Auvity (2002) identified the formation of an instability on the piston vortex. The instability possessed a well-defined wavelength. The instability appeared to be forming on the outer turn of the piston vortex rather than in the core. It was postulated that this instability was centrifugal in nature and satisfied the criteria for the instability of a wall jet on a concave surface, as described in Floryan (1986).

In a broader contex this class of transient vortical structure also occurs in shear- or lid-driven cavity flows. As the shear layer or moving lid interacts with the downstream corner of the cavity, a transient vortical roller is formed which eventually leads to a steady rotational cavity flow. Cavity flows exhibit a range of steady topologies depending on the cavity Reynolds number. Typically the flow is described in terms of a primary eddy and viscous corner eddies; see Pan & Acrivos (1967). The primary eddy is the analogue of the junction vortex described in the current paper. Cavity flows of sufficiently high Reynolds number display an instability that has been labelled Taylor–Görtler-like (TGL); see Koseff & Street (1984*a*) and Aidun, Triantafillopoulos & Benson (1991). The mechanism for the formation of these instabilities has been attributed to the concave region that exists between the primary vortex and the viscous corner eddy. The linearised instability calculations of Albensoeder, Kuhlmann & Rath (2001), for a cavity with a large depth-to-width ratio, indicate that the region of high shear between the primary inviscid eddy and the separation point on the rigid wall, downstream of the moving lid, is a region of high streamline curvature and velocity gradients and a source of centrifugal instability. However, in cavity-flow studies little attention has been paid to the development of spanwise instabilities during the transient start-up. Koseff & Street (1984) identified an instability on the transient structure that they classified as Taylor cells and noted that the wavelength of the instability at this point was different from its value when the cavity reached a steady-state condition. Vogel, Hirsa & Lopez (2003) and Blackburn & Lopez (2003) examined the stability of cavity flows driven by a lid moving in a sinusoidal form. Vogel, Hirsa & Lopez (2003) noted the formation of spanwise cellular instabilies, in the shear layer that wraps around the primary vortex roller. These structures appear qualitatively similar to the piston vortex instability observed by Allen & Auvity (2002). The formation of these instability structures in Vogel *et al.* (2003) was dependent on the Reynolds number, $Re_H = U_{max} H/\nu$, where H is the cavity depth. They estimated that the Reynolds number for transition in the steadily driven wall case, i.e. as $T \rightarrow \infty$ where T is the floor period, was $Re_H \simeq 325$, which is in agreement with the stability calculations of Albensoeder & Kuhlmann (2002). Blackburn & Lopez (2003) utilized Floquet analysis to study the development of these instabilities. They found that the primary vortex is unstable to two synchronous modes, a long-wavelength mode that scales as the size of the vortex core and a short-wavelength instability formed on the shear layer wrapped around the vortex roller. The short-wavelength instability was classified as centrifugal, scaling as the vorticity thickness of the shear layer and similar in form to the braid-type streamwise instabilities that form in between the rollers of a shear layer. A general conclusion that can be drawn from these instability

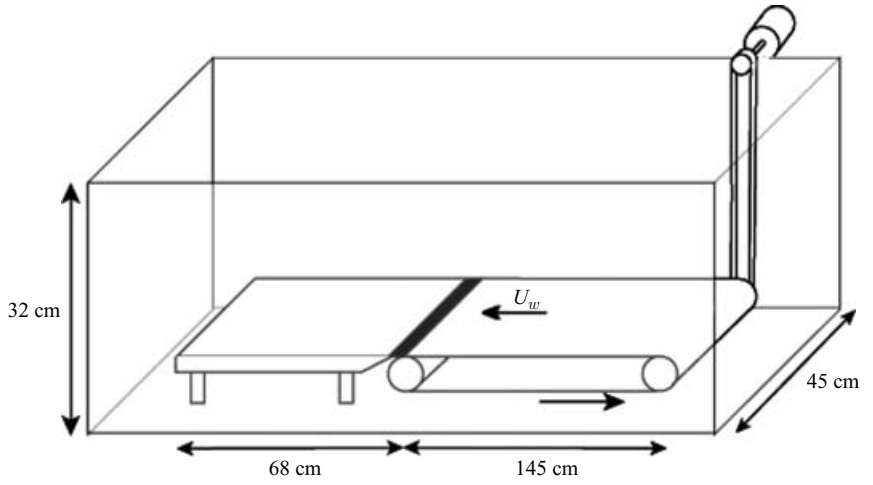

FIGURE 2. Schematic of the experimental apparatus.

studies is that secondary vorticity that forms on wall surfaces to enforce the no-slip condition is prone to separate if the Reynolds number is high enough and that these layers of secondary vorticity are prone to centrifugal instabilities.

The goals of the current study are to examine the formation of the transient structure mentioned above, in an experimental configuration where apparatus length scales are absent, to test for self-similar behaviour and to classify the transition mechanism of three-dimensional instabilities on the primary vortex structure.

2. Experimental apparatus

The experimental apparatus consisted of a moving left 30 cm wide and 150 cm long. The belt fully immersed in a water tank, was set in motion with a programmable stepper motor. The stationary plate consisted of an acrylic sheet, with an edge angle machined to 15 degrees. Attached to the edge was a 0.015 cm thick, 2.5 cm wide strip of brass. During experiments the shim was in contact with the moving belt and formed a junction with minimal step. The dimensions of the apparatus ensured that the spatial scale of a vortex cross-section, $0.5 \rightarrow 5$ cm was almost an order of magnitude smaller than the width and depth of the tank. Experiments were conducted in both water and air to achieve a large Reynolds-number range. A schematic of the apparatus is shown in figure 2.

The range of developing Reynolds number Re_Γ achievable with this apparatus was $5 \times 10^2 < Re_\Gamma < 5 \times 10^5$. This range of Reynolds numbers allows observation of the transition of the structure from laminar to turbulent behaviour. For the experiments in water the fluid temperature was maintained at $21 \pm 0.5^\circ$C (laboratory temperature). It was necessary to have the temperature differential between the tank and surroundings as small as possible, as the vortex trajectory was found to be very sensitive to the presence of temperature-gradient-induced convection. It was noted that if the junction between the plate and belt was poor, i.e. if a gap existed or the thickness of the lip on the stationary plate was the order of the boundary-layer thickness, a Kelvin–Helmholtz-like instability would appear on the outer turn of the vortex. By making the lip from shim stock and having it in continual contact with the moving plate this instability was suppressed. The driving belt was a tensioned

rubber belt one-quarter of an inch thick. The surface of the belt was smooth, with a mean roughness amplitude of 0.05 mm, significantly smaller than the shim-stock thickness. The experimental technique involved using a laser sheet generated with an argon-ion laser. Fluorescent dye and smoke were used to visualize the motion and size of the vortex core and particle-image velocimetry (PIV) data was collected to provide information about the velocity field of the vortex.

3. Results

3.1. *Self-similarity of the junction vortex*

During an experiment, the circulation swept into the junction region can be defined as $\Gamma(t) = \int_0^t U_w^2(\tau)\mathrm{d}\tau$. This results in a Reynolds number, or non-dimensional time, defined as $Re_\Gamma = \Gamma(t)/\nu$. In the case of constant wall velocity this expression reduces to $Re_\Gamma = U_w^2 t/\nu = U_w L/\nu$. Figure 3 shows flow visualization images at moderate Reynolds numbers, $4 \times 10^3 < Re_\Gamma < 20 \times 10^3$. The images were obtained for three different wall speeds. For each speed, images were selected for the same four values of Re_Γ. The images have been scaled by the same non-dimensional spatial scale, defined as $r^* = rU_w/\nu$. A movie of the $U_w = 35\,\mathrm{mm\,s^{-1}}$ images the online is available with/version of the paper (movie 1).

It is apparent that at each Reynolds number the visualizations from the three different wall speeds appear to have the same shape and number of turns on the vortex; this is a qualitative indicator of self-similarity. They suggest that the flow field is universal for a given Re_Γ when the dimensions of the structure are non-dimensionalized with U_w/ν and the velocity is non-dimensionalized with U_w. The visualizations at $Re_\Gamma = 24 \times 10^3$ (figure 3) show signs of three-dimensionality on the outer turn of the vortex, in the region of high shear that separates the rapidly rotating fluid from the moving wall and the fluid that was initially at rest over the stationary plate. This waviness is an indicator of instability development, discussed in § 4. Figure 4 shows for comparison flow visualizations in water and in air at $Re_\Gamma = 4 \times 10^3$. Although there is an eight-fold difference in spatial scale between these two images, when scaled with U_w/ν the structures appear to have a self-similar shape.

A feature of all these visualizations, at moderately high Reynolds numbers, is that the separation point, defined as the location where the dye streak-line leaves the stationary plate and moves along the plate, is located directly under the vortex core. It may be postulated that this point represents the region of maximum adverse pressure gradient on the plate owing to the presence of the separated vortical structure above it. There is no region of reversed flow on the stationary plate and so the separation point is an unsteady one. Quantitative information from the flow visualizations includes measures of the size of the developing structure. Figure 5 shows a cross-section of the vortical structure with the core location, labelled as (X_Γ, Y_Γ), and measures of the dimensions of the vortical structure, labelled as X_D and Y_D. The origin of the coordinate system to measure the location of the vortex core was set at the junction of the moving wall and the stationary wall.

Measurements of these various length scales were obtained from video images of the experiments. The start time of the motion of the belt was determined from a LED that was in view and turned off when the belt motion commenced. Figure 6 shows data for the vortex core scaled with respect to U_w/ν and plotted against Re_Γ. The data shows good universal collapse over a large range of Re_Γ. For the experiments conducted in air the data for Y_Γ can be seen departing from the universal curve in the

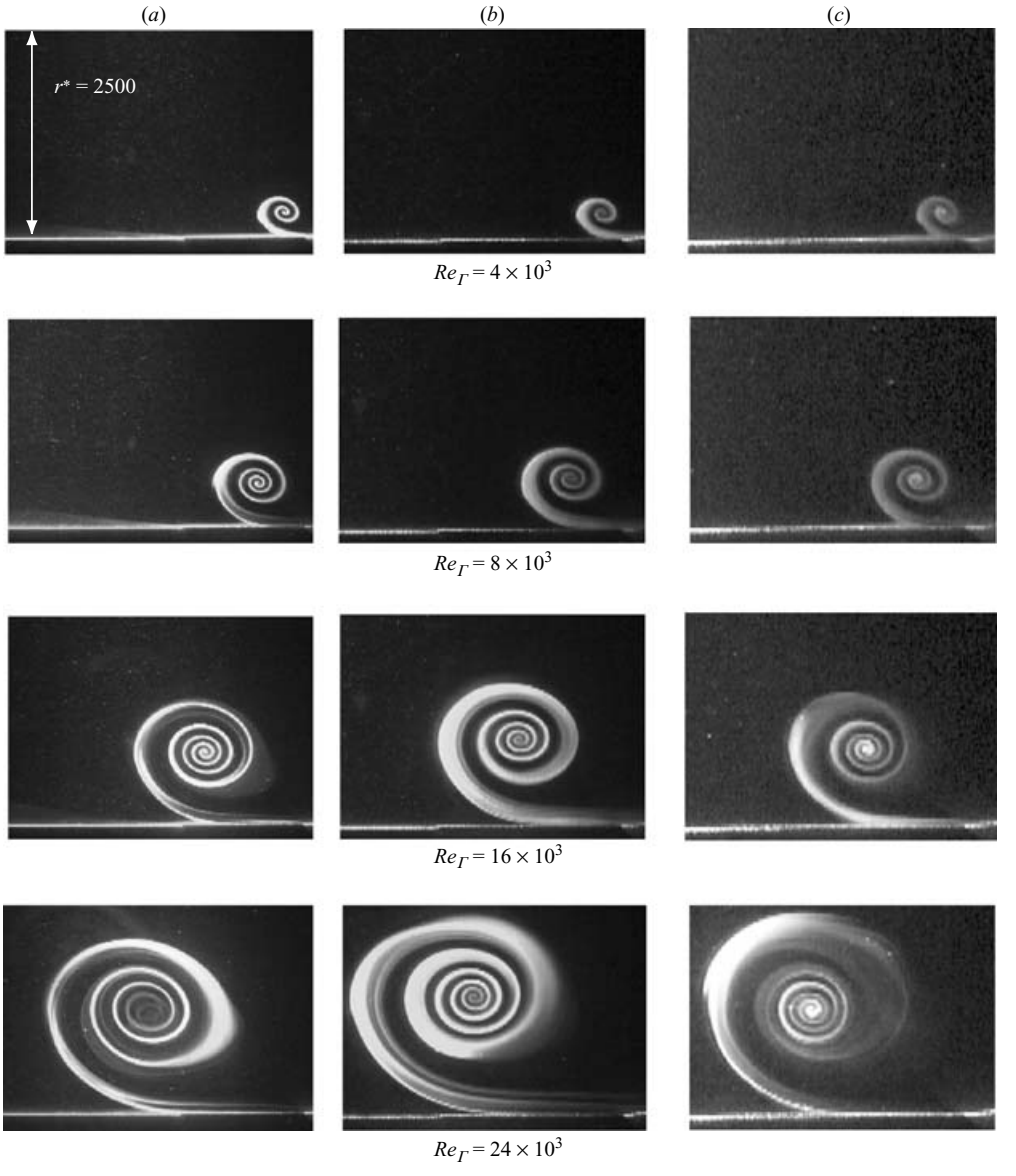

FIGURE 3. Visualization of vortex development at the junction of a moving and a stationary surface for wall speeds (*a*) $U_w = 35\,\mathrm{mm\,s^{-1}}$, (*b*) $U_w = 69.5\,\mathrm{mm\,s^{-1}}$ and (*c*) $U_w = 103\,\mathrm{mm\,s^{-1}}$ over a range of Re_Γ.

later stages of the experiments. This occurs when the size of the structure approaches the depth of the tank, which inhibits the growth of the vortex in the vertical direction. Figure 7 shows data for the diameter of the vortex core, scaled with respect to U_w/ν and plotted against Re_Γ. Again it appears that the collapse of the data is universal over a significant Reynolds-number range.

Power-law fits to the data of the form

$$(X_\Gamma, Y_\Gamma)U_w/\nu = \kappa Re_\Gamma^q = \kappa\left(U_w^2 t/\nu\right)^q \tag{3.1}$$

are shown fitted to the data of figures 6 and 7 and the results are listed in table 1.

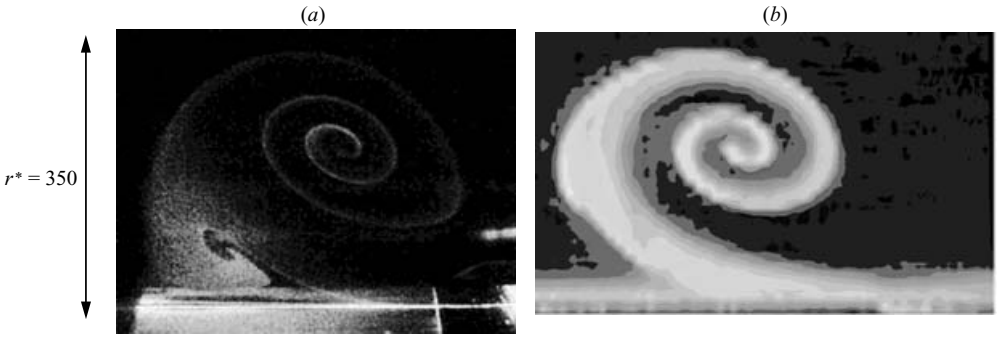

FIGURE 4. Visualizations of vortex development at $Re_\Gamma = 4 \times 10^3$ in (*a*) air and (*b*) water.

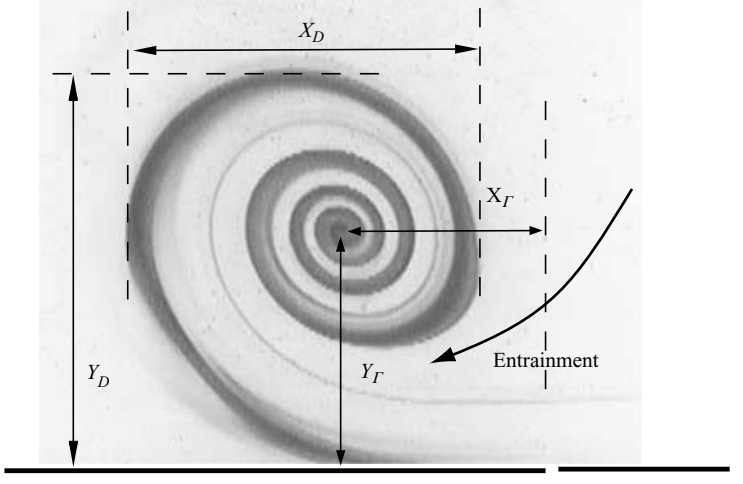

FIGURE 5. Definition of spatial scales.

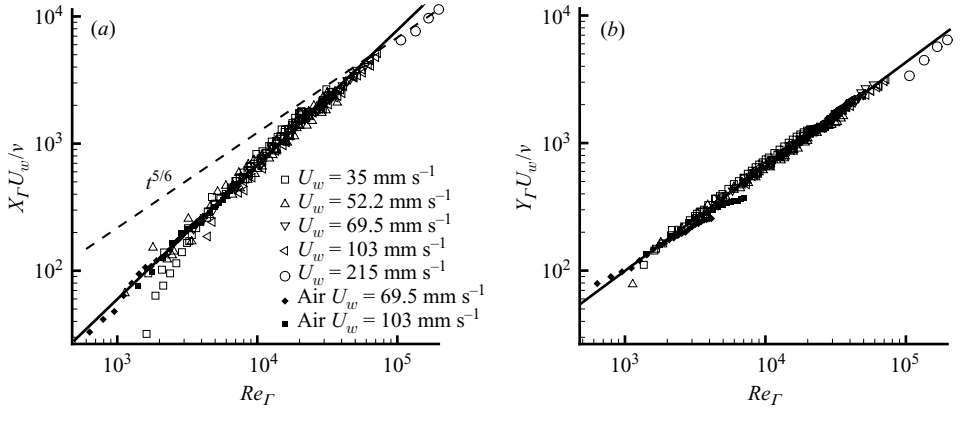

FIGURE 6. Scaling of (*a*) the X_Γ coordinate and (*b*) the Y_Γ coordinate of the vortex core with respect to U_w/ν, plotted against Re_Γ.

	X_Γ	Y_Γ	X_D	Y_D
q	1.05	0.813	0.89	0.867
κ	0.043	0.366	0.254	0.32

TABLE 1. Scaling-law fits.

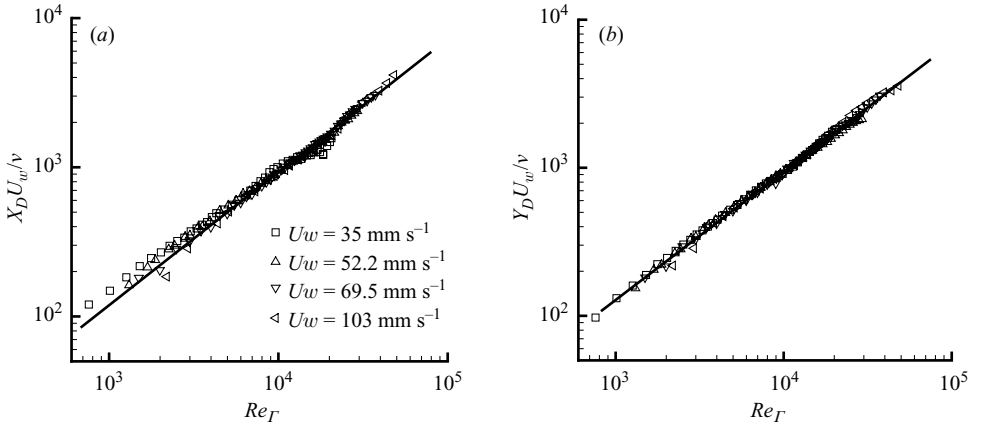

FIGURE 7. Scaling of (*a*) the X_D coordinate and (*b*) the Y_D coordinate of the vortex core with respect to U_w/ν, plotted against Re_Γ.

The vortex appears to be growing in size at a universal rate in the vertical and horizontal directions, as shown by the universal collapse of the data for X_D and Y_D with the same scaling, $t^{5/6}$. It appears, however, that the vortex core X_Γ moves along the plate at a slightly faster rate, t. This would indicate that similarity scaling does not apply to coordinates used to describe the location of the vortex core. For comparison, figure 6(*a*) also shows the curve $t^{5/6}$ fitted to the data for X_Γ. While it would appear that this curve is not appropriate at low Re_Γ, it does start to fit the data well as the Reynolds number increases. The growth rates of all scales are significantly faster than the viscous rate $t^{1/2}$, indicating that the structure is not a viscous bubble. To illustrate this point, data for the vortex size is scaled against $\sqrt{\nu t}$ and plotted against Re_Γ in figure 8.

The location of the vortex core and Re_Γ can be measured to better than 5 % accuracy from videotape; however, the significant source of error comes from the variation between experiments. Each plot in figures 6–8 contains data sets from multiple experiments at the same experimental conditions. The spread of the data reflects the size of the experimental error. The error in X_Γ, the most sensitive measure, is of order 20 % while the error in the measures for Y_Γ, X_D and Y_D appears to be of order 10 %.

Conlon & Lichter (1995) found that if the strength of the vorticity in the wall layer was not sufficient in relation to the outer layer of vorticity then a monopole structure forms and propagates along the stationary wall with relatively little growth away from the wall. Conlon & Lichter (1995) suggested that the formation of a dipole structure is characterized by a roll-up of the wall layer, which results in a divergence of the dipole away from the surface. In the current experiments, while the vortex

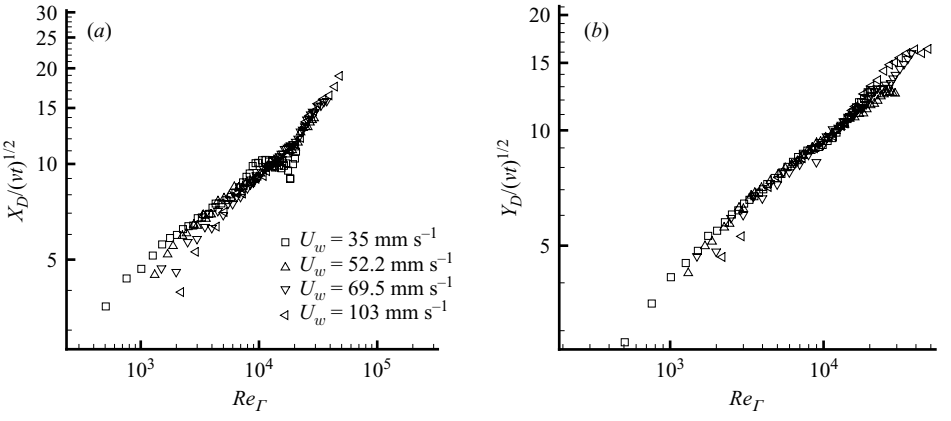

FIGURE 8. Scaling of (*a*) X_D and (*b*) Y_D with respect to the viscous length scale $\sqrt{vt}$, plotted against Re_Γ.

structure resembles a monopole and there is no indication of the roll-up of vorticity from the stationary surface, there is a strong growth of the primary structure away from the wall. This perhaps indicates the subtle effect of the time-varying strength of the vorticity that is being convected into the junction region from the Stokes layer.

A possible source of lack of similarity in the data for the measurement of the vortex core coordinate, X_Γ, is due to the assumption that the origin of the structure is the junction of the moving belt and the stationary one. The problem of locating the virtual origin of the similarity structure was encountered in the experimental studies of both Cantwell, Coles & Dimotakis (1978) and Glezer & Coles (1990). In the case of the turbulent-spot experiment of Cantwell *et al.* (1978), as the boundary-layer growth is parabolic the region of observed linear growth of the structure corresponds to a range where the linear and parabolic curves overlap. Cantwell *et al.* (1978) used experimental data to extrapolate upstream to determine the virtual origin of the turbulent spot. In a similar vein, the turbulent-vortex-ring study of Glezer & Coles (1990) used experimental data to extrapolate and determine the virtual origin of a growing turbulent vortex ring, as such a vortex ring possesses an initially laminar phase which is not described by similarity scaling.

In the current study it has been noted that as the Reynolds number becomes large the X_Γ coordinate of the vortex core appears to approach a $t^{5/6}$ scaling. This in turn suggests that the origin used to measure the location of the structure may be incorrect. In order to locate the 'virtual' x origin of the structure, curves of the form $X_\Gamma U_w/\nu - \beta$ were fitted to the data for the vortex core and plotted against Re_Γ. Figure 9 shows a plot of $X_\Gamma U_w/\nu = 0.42 Re_\Gamma^{5/6} - 150$ overlaid on the experimental data. The collapse of the experimental data onto this curve is good, which suggests that the universal origin for this structure is offset from the junction singularity by a distance $X_o = -150\nu/U_w$.

In conclusion the results from the flow-visualization data at intermendiate Reynolds numbers indicate that the size and location of the vortex scales as $t^{5/6}$. The data for core location collapses are universally and the independent of the fixed-apparatus dimension when scaled with U_w/ν and plotted against Re_Γ. The non-dimensional origin of the vortex during this universal behaviour is $X_o = -150\nu/U_w$.

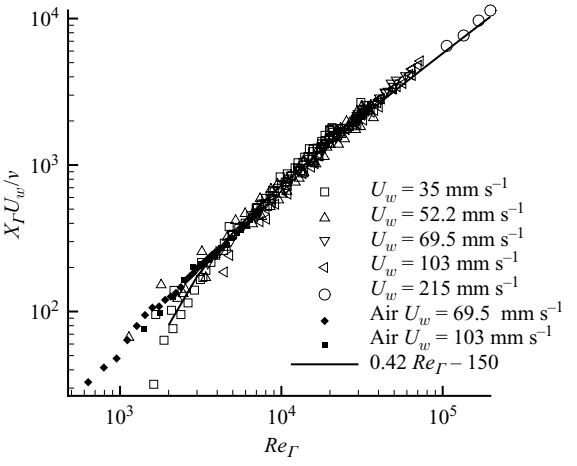

FIGURE 9. Determination of the virtual origin of the vortex core.

3.2. *PIV results*

Particle-image velocimetry experiments were performed to generate quantitative velocity and vorticity fields during vortex development. The data-acquisition system consisted of an argon-ion laser, an externally triggered Cohu 6600-3000 digital camera, a General Scanning 6120DT series oscillating mirror and an Epix frame grabber. Details of the PIV-system hardware and software, which is capable of a minimum time difference between images equal to 0.5 ms, are contained in Allen & Smits (2001). Figure 10(*a*) shows a sequence of velocity fields for a wall speed of 52 mm s^{-1} in water for a range of Re_Γ. The defining feature of these patterns is the developing rotational core of the vortex. The region of high shear between the separating vortex and the stationary wall is evident from the velocity field and is highlighted in figure 10(*a*) for $Re_\Gamma = 8 \times 10^3$. It is also evident from these velocity fields that there is no region of reversed flow over the stationary plate. Figure 10(*b*) shows the vorticity fields associated with the velocity fields. The plots show the non-dimensional vorticity, $\omega = \Omega\nu/U_w^2$. They have two important features: the rolling-up of the Stokes-layer vorticity from the moving wall into a coherent spiral, and the production of strong secondary vorticity on the stationary plate. The vorticity distributions do not show any evidence of dipole formation. As mentioned earlier the secondary vorticity is generated to preserve the no-slip condition over the stationary plate. Figure 11 shows contour plots of velocity magnitude normalized with U_w, for three different wall speeds at $Re_\Gamma = 8 \times 10^3$ and at $Re_\Gamma = 16 \times 10^3$. The plots have been scaled spatially with U_w/ν. The plots at equal Re_Γ show similar shapes and distributions of non-dimensional velocity. The plots for the lowest wall speed show better resolution, as the physical scale of the vortex is larger than for the higher-wall-speed cases.

3.3. *Dynamics*

The questions that arise from experimental core and PIV data are:

(i) under what condition will a vortex form?

(ii) can the observed growth rates be related to the dynamics of the structure formation?

In order to explain the formation process a description is required that begins with the low-Re_Γ viscous-dominated flow before transitioning to the high-Re_Γ inertia-dominated flow. Cantwell (1986) considered the transient motion of a viscous fluid

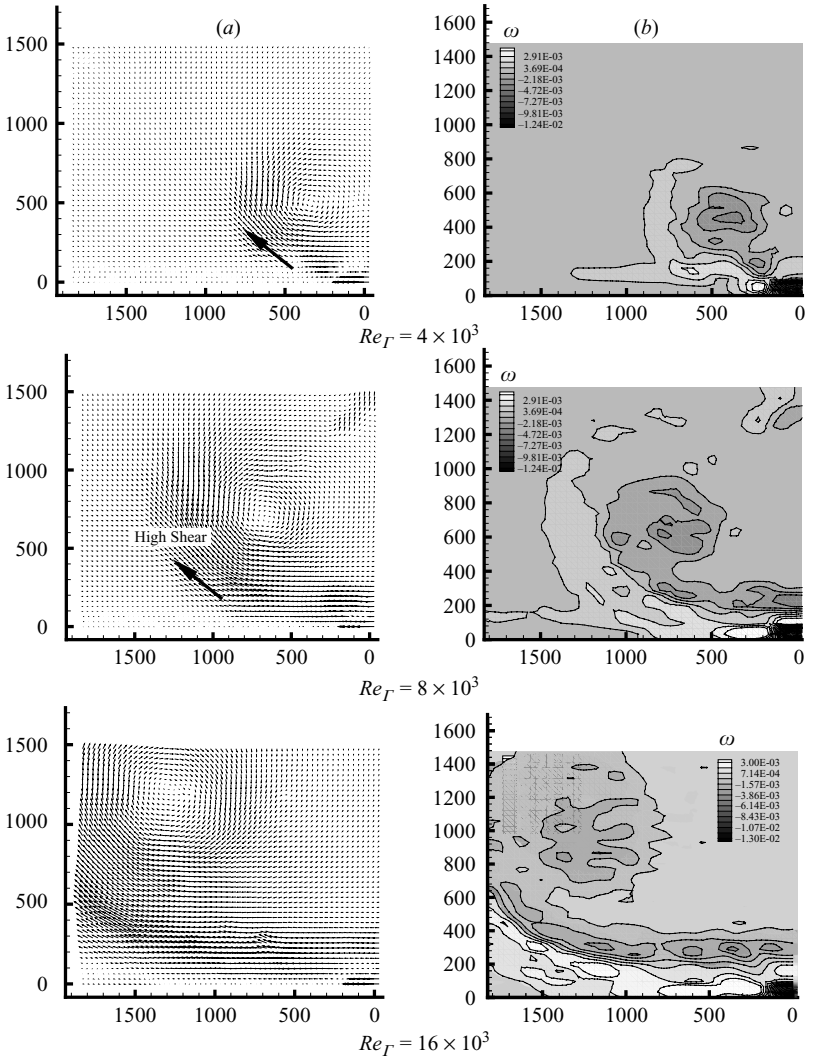

FIGURE 10. (*a*) Velocity and (*b*) vorticity fields for a wall speed $U_w = 52\,\mathrm{mm\,s^{-1}}$ at $Re_\Gamma = 4000, 8000, 16\,000$.

forced from an initial state of rest in an effort to clarify the events leading to the characteristic vortical structure at the head of the jet. A key element in this analysis was the absence of apparatus-length scales. In the planar analysis Cantwell considered the jet to be produced by a time-varying point force applied at the domain origin, defined as $F(x, y; t/\rho) = (Mf(t)\delta(x)\delta(y), 0)$, directed along the x axis. The associated impulse of the jet was computed as the integal of the forcing function. The quantity M is a force-amplitude parameter and has the dimensions L^3T^{-n}. The impulse applied to the flow is $I(t) = Mt^{(n-1)}/(n-1)$. Selection of the type of forcing to produce the jet – impulse, step or ramp then defines the value of the exponent n. Cantwell utilized similarity groups to render the Stokes equations and the applied impulse invariant under transformation, in order to reduce the number of independent variables needed to describe the system. Cast in terms of similarity variables, the Stokes equations were found to depend on a control parameter Re_I, which is defined in terms of the impulse

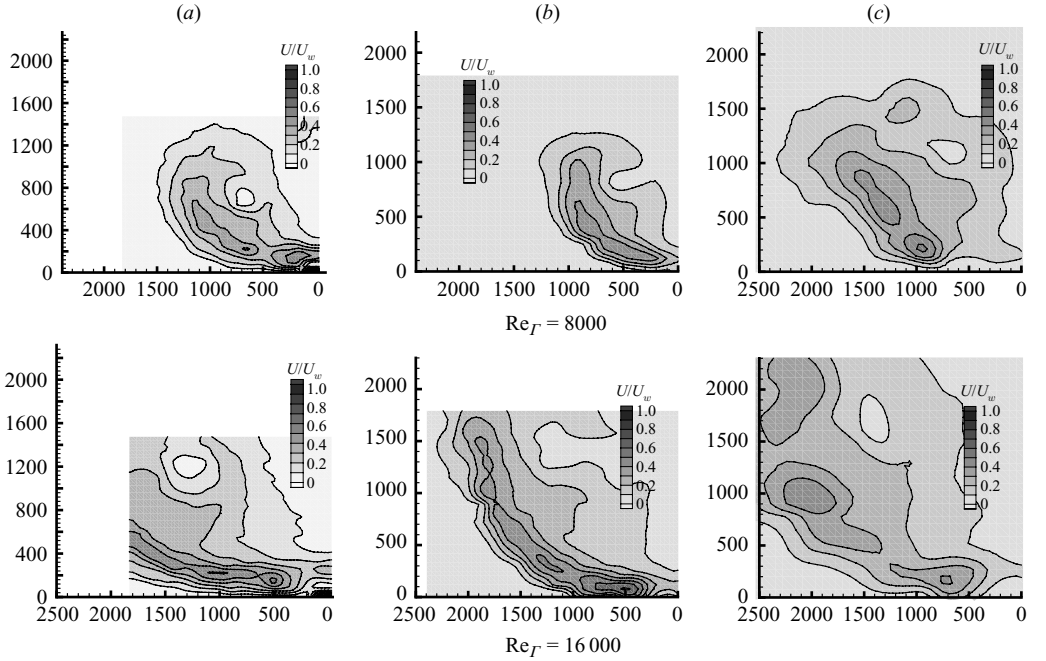

FIGURE 11. Normalized velocity fields for (*a*) $U_w = 52\,\mathrm{mm\,s^{-1}}$ and (*b*) $U_w = 69.5\,\mathrm{mm\,s^{-1}}$ and (*c*) $103\,\mathrm{mm\,s^{-1}}$ for $Re_\Gamma = 8000$ and $Re_\Gamma = 16\,000$.

that has been applied to the flow: $Re_I = (I(t)t)^{2/3}/(4\nu t) = M^{2/3}t^{2n/3-1}/((n-1)^{2/3}4\nu)$. When considering the evolution of a self-similar structure, particle pathlines or entrainment diagrams are very useful for identifying a change in the flow topology. Substituting similarity variables into the expressions for the unsteady trajectory of the particles, Cantwell produced a set of coupled linear equations where the critical points and characteristics in similarity variables were functions of the parameter Re_I. He solved for three different flow topologies as a function of two critical Re_I parameters. These Reynolds numbers represented bifurcation boundaries. As mentioned earlier, the first bifurcation marks the point when the jet transitions from a non-rotating slug, which in the entrainment diagram is manifested as a single node, to a topology that consists of an on-axis saddle and off-axis nodes. For a constant impulse jet this occurs at $Re_I \simeq 1.2$. The second bifurcation point is at the transition of the off-axis nodes into foci at $Re_I \simeq 2.2$. It is this second transition which produces the characteristic evolving mushroom at the head of the jet. Cantwell showed that a similar procedure, based on the lack of an experimental length scale and applied-impulse invariance, could be used to develop similarity groups that rendered the Euler equations, and the impulse, invariant to transformation. The forms of these similarity groups are

$$\xi = \frac{x}{M^{1/3}t^{n/3}}, \qquad U(\xi) = \frac{u}{M^{1/3}t^{1-n/3}}, \qquad P(\xi) = \frac{p/\rho}{M^{2/3}t^{2(n/3-1)}}, \tag{3.2}$$

where M is the force-amplitude parameter and the exponent n again is defined by the nature of the forcing. As the Reynolds numbers for the current experiments are high, it would be expected that inertial effects would dominate the flow.

The point source of momentum and the absence of experimental length scales in Cantwell (1986) are different boundary conditions from that of the current experiment;

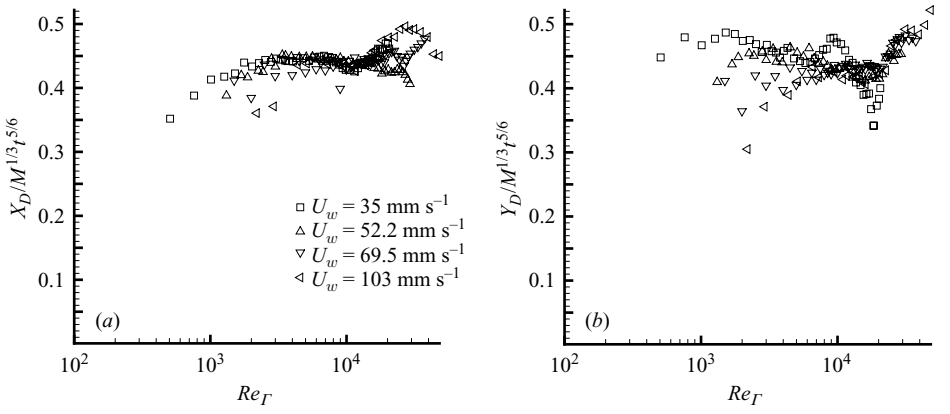

FIGURE 12. Self-similar scaling to collapse the vortex-diameter data.

however, many features of the current study display starting-jet characteristics. If one considers the current transient problem with boundary conditions $U(x, y) = 0$, $t < 0$, $U(|x| < X/2, 0) = U_w$ and $U(|x| > X/2, 0) = 0$ for $t > 0$ this corresponds to a moving wall of finite length X in an infinite domain. The moving wall acts as a soure of momentum via the action of the shear force through the Stokes-layer forming over the plate. The stationary plate will act as a momentum sink, and in the far field one would expect the flow field to have the form of a dipole. As the impulse is being imparted by the moving wall, a crude approximation for the momentum being created can be derived from a Stokes-layer description of the velocity field. The rate of flux of momentum into the corner junction can be derived from

$$\mathrm{d}M_{mtm}(t)/\mathrm{d}t = \int_0^\infty U^2_{Stokes}(y, t)\,\mathrm{d}y, \tag{3.3}$$

where y is the wall-normal distance. Using the analytic expression for the velocity layer forming over an impulsively started plate, (3.3) can be reduced to

$$M_{mtm}(t) = 4.256\sqrt{\nu}U_w^2 t^{3/2}. \tag{3.4}$$

From Cantwell (1986), a Reynolds number based on impulse is $Re_I = (I(t)t)^{2/3}/(4t\nu)$. Substitution of the approximation for the impulse that the moving belt applies to the flow and assuming symmetry across the x axis results in

$$Re_I = 0.656\left(U_w^2 t/\nu\right)^{2/3} = 0.656\,Re_\Gamma^{2/3}. \tag{3.5}$$

If we relate the predicted momentum flux to the impulse $I(t) = Mt^{(n-1)}/(n-1)$ it implies that $3/2 = n - 1$, hence $n = 5/2$. Physically this means that the action of the moving plate is midway between a steady jet and a ramp jet. It also results in a definition of M:

$$M = 6.384\sqrt{\nu}U_w^2. \tag{3.6}$$

Using the estimation for the applied impulse results in an explicit set of similarity groups for the junction flow at high Reynolds numbers,

$$\xi = x/\left(M^{1/3}t^{5/6}\right), \qquad \eta = y/\left(M^{1/3}t^{5/6}\right), \qquad U = u/\left(M^{1/3}t^{-1/6}\right). \tag{3.7}$$

This analysis suggests that the spatial scale of the flows should develop as $t^{5/6}$, which is very close to the experimental data for the core diameter. Figure 12 shows

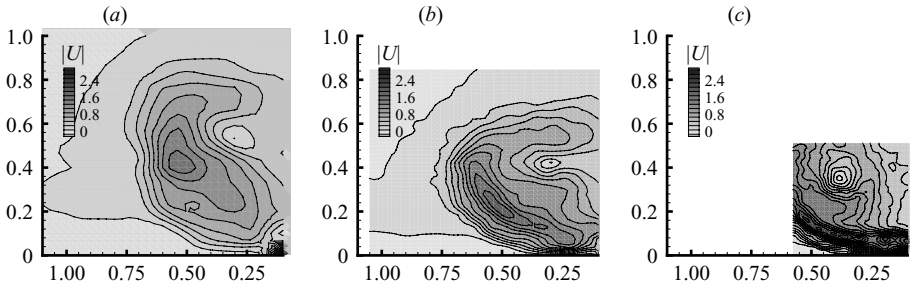

FIGURE 13. Velocity-field contours using similarity scaling for $U_w = 52\,\mathrm{mm\,s^{-1}}$: (*a*) $Re_\Gamma = 4000$, (*b*) 8000 and (*c*) 16 000.

data for the vortex diameter scaled with $0.54M^{1/3}t^{5/6}$. The collapse is good for a given Re_Γ, and the data appears to be invariant with respect to Re_Γ, as predicted for high-Reynolds-number flows.

As well as collapsing the flow-visualization data, this high-Reynolds-number scaling argument also suggests that the velocity fields scale as $M^{1/3}t^{-1/6}$. The plots in figure 13 show velocity data for three Reynolds numbers, scaled as $U = u/(0.53M^{1/3}t^{-1/6})$. The spatial scale has been transformed using $\xi = x/(0.53M^{1/3}t^{5/6})$ and $\eta = y/(0.53M^{1/3}t^{5/6})$ with the origin adjusted as described above.

All three plots show a vortex core and a region of high shear between the vortex core and the wall boundary. The vortex-core location for the $Re_\Gamma = 4000$ case does not appear to have reached a constant value. For the $Re_\Gamma = 8000$ and 16 000 cases the vortex core appears to be located at (0.35, 0.4). The trend for all three cases is for the region of high-intensity velocity contours separating the vortex core from the stationary boundary to become smaller as Re_τ increases. This may indicate a progression toward a universal self-similar shape which is independent of Reynolds number as the Reynolds number becomes high enough. It is suggested that the rate at which the velocity magnitude approachs its asymptote is slightly slower than the rate at which the shape appraches its limit. In conclusion, self-similarity scaling, derived from Euler's equations, has been relatively successful in collapsing the experimental data to produce a universal description of the flow structure. The lack of exact self-similarity is thought to be due to finite-Reynolds-number effects.

3.4. *Entrainment diagram*

One problem with the interpretation of contour patterns of velocity fields or streamline patterns is that their form depends on the translation velocity of the observer. However, if self-similarity applies, a universal, invariant, picture of the flow field can be obtained from a description of the particle trajectories. The particles in this sense are assumed to be passive, ideal, massless and to track the flow field exactly. The equations for two-dimensional particle paths in physical coordinates are expressed as

$$\mathrm{d}x/\mathrm{d}t = u(x, y, t), \qquad \mathrm{d}y/\mathrm{d}t = v(x, y, t), \tag{3.8}$$

which can be recast in terms of the suggested similarity variables (equations (3.7)) as

$$\mathrm{d}\xi/\mathrm{d}\tau = U(\xi, \eta) - (5/6)\xi, \qquad \mathrm{d}\eta/\mathrm{d}\tau = V(\xi, \eta) - (5/6)\eta \tag{3.9}$$

Cantwell (1986) showed that the entrainment diagram is invariant with respect to a translation velocity commensurate with the similarity scaling, i.e. if a translation

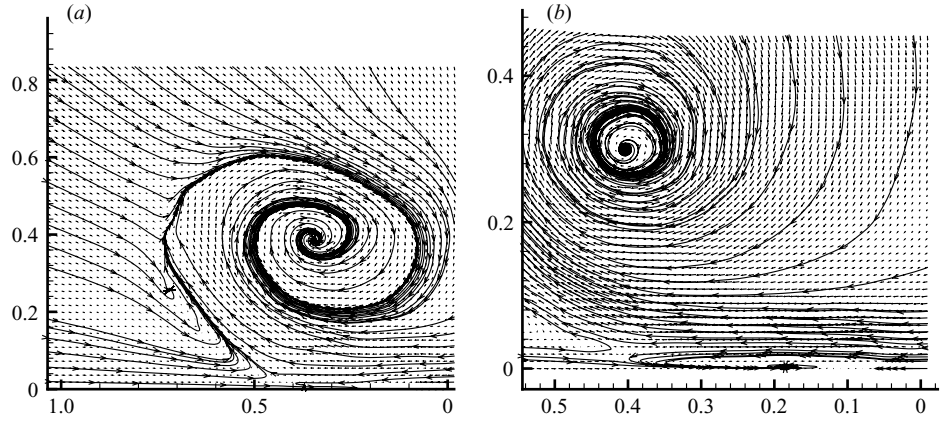

FIGURE 14. Entrainment diagram for $U_w = 52.2\,\mathrm{mm\,s^{-1}}$ at (*a*) $Re_\Gamma = 8000$ and (*b*) $Re_\Gamma = 16\,000$.

defined as

$$x_i = \hat{x}_i - \alpha M^{1/3} t^{5/6}, \qquad t = \hat{t}, \qquad u_i = \hat{u}_i - (5/6)\alpha M^{1/3} t^{-1/6} \tag{3.10}$$

is applied to the data then the equation for particle paths, $\mathrm{d}\hat{\xi}/\mathrm{d}\hat{\tau} = \hat{U}(\xi) - (5/6)\hat{\xi}$, still has the same form as (3.9) and the entrainment diagram is invariant translation. The equations for particle trajectories are invariant with respect to the time-evolving Reynolds number, as they were derived from Euler's equations. This is indicated in the Reynolds-number invariance of the contour plots in figure 13. While we are not in a position to solve these equations analytically, we can construct a picture of the entrainment diagram via a technique of isolines applied to the experimental data, as described in Cantwell *et al.* (1978) and Glezer & Coles (1990). Figure 14 shows entrainment diagrams for $Re_\Gamma = 8000$ and 16 000, for a wall speed of $U_w = 52.2\,\mathrm{mm\,s^{-1}}$, generated using the technique of isolines applied to the PIV data. The essential feature of both these plots is a focus. Figure 14(*a*) shows a focus located at $(\xi, \eta) \simeq (0.38, 0.38)$ and what appears to be a saddle located on the horizontal axis at approximately $\xi \simeq 0.48$. The entrainment diagram bears a strong resemblance to the final entrainment diagram of the viscous jet of Cantwell (1986). Figure 14(*b*) provides better spatial resolution of the entrainment pattern and shows a focus at $(\xi, \eta) \simeq (0.40, 0.30)$. The difference between figures 14(*a*) and 14(*b*) is thought to be a function of cycle-to-cycle experimental variation. Figure 14(*b*) also allows one to make an accurate assessment of the topology close to the wall. Figure 14(*b*) shows the presence of a saddle, located a short distance away from the stationary wall surface at $(\xi, \eta) \approx (0.4, 0.03)$; the junction singularity appears as a node at $(\xi, \eta) = (0.2, 0)$.

A graphical interpretation of the self-similar entrainment diagram is shown in figure 15. The essential features are a node *A*, a saddle *B* and a focus *C*. The particle pathlines indicate that the majority of fluid is entrained into the vortex core through the rear of the vortex. There is, however, a finite amount of fluid, close to the stationary plate surface, that is not entrained into the vortex core. This is the viscous boundary-layer that is developing over the stationary plate. This material appears to be heading towards the junction singularity, which appears as a sink node when viewed in similarity coordinates. Hence, in conclusion, the development process for the junction vortex is a progression from an initially viscous-dominated flow to an inertially dominated structure for $Re_\Gamma > 1000$. The final self-similar entrainment

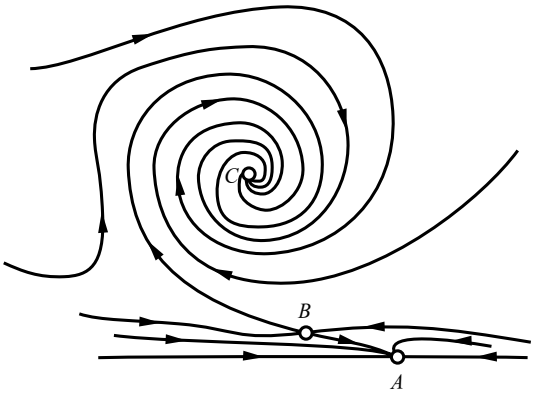

FIGURE 15. Interpretation of a self-similar entrainment diagram at high Re_Γ.

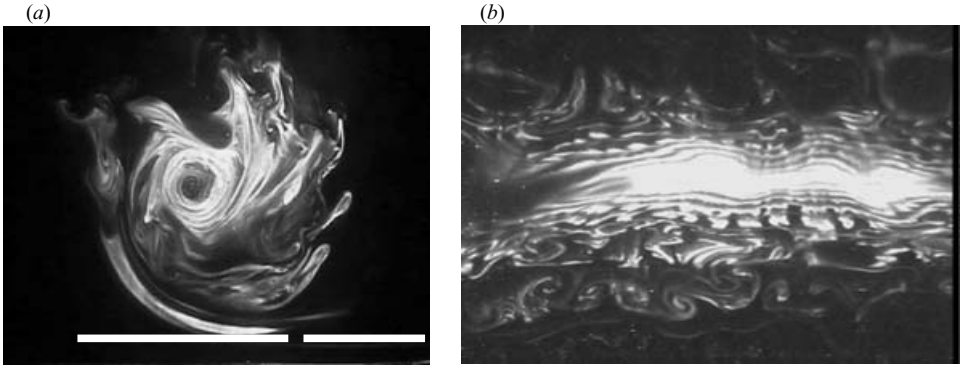

FIGURE 16. Turbulent vortex at $Re_\Gamma = 110 \times 10^3$: (*a*) streamwise cross-section and (*b*) spanwise cross-section.

diagram, for high Reynolds numbers, bears a strong resemblence to the topology identified by Cantwell (1986) as representing the commencement of the characteristic rotational instability at the head of a viscous jet. It is conjectured that for $Re_\Gamma < 1000$ one should observe on evolving flow topology similar to that identified by Cantwell (1986), i.e. if the Reynolds number is low enough one should observe a the variation in the flow topology from a non-evolving vortex front into the spiral structure observed in the current experiments. The control parameter for this process is the time-evolving Reynolds number, which can be related to the impulse that the plate has applied to the flow. A limitation of the current experiments is that the minimum Re_Γ is too high to investigate this regime. It is suggested that a direct numerical simulation would be the best way to approach this low-Re_Γ range.

4. Instability development

4.1. *Flow visualisation*

At $Re_\Gamma \simeq 20 \times 10^3$ waves begin to appear on the outer turn of the vortex structure, as illustrated in figure 1(*b*). The amplification of these waves leads to the eventual transition to a fully three-dimensional structure at $Re_\Gamma \simeq 40 \times 10^3$. Figure 16(*a*) shows a strongly three-dimensional vortex, at $Re_\Gamma = 110 \times 10^3$, which is entraining fluid around its perimeter. Figure 16(*b*) shows a spanwise visualization through the core

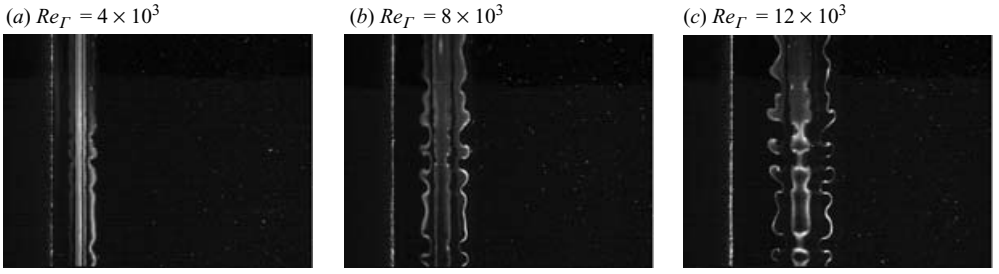

FIGURE 17. Developing instability for a wall speed $U_w = 35\,\mathrm{mm\,s^{-1}}$ at (*a*) $Re_\Gamma = 4 \times 10^3$, (*b*) $Re_\Gamma = 8 \times 10^3$ and (*c*) $Re_\Gamma = 12 \times 10^3$.

of the vortex. The transition to turbulence of the piston vortex was remarked on by Tabaczynski *et al.* (1970), but no detailed description of a transition mechanism was provided. Unstable waves were observed by Allen & Auvity (2002) on the vortex forming in front of a moving piston, and the suggested mechanism for the formation of these instabilities was centrifugal. In the context of start-up cavity-flow experiments Koseff & Street (1984*b*) noted that during the cavity start-up the junction vortex, described as a 'cylinder of high vorticity fluid', became unstable. Torroidal vortices were observed by Koseff & Street (1984*b*) on the periphery of the main vortex core and they noted that the wavelength of the instability decreased as their belt speed increased. In order to examine the detailed structure of the instability, a laser cross-section was taken in a plane inclined at 43° to the moving wall. The laser was used to illuminate a spanwise slice through the vortex. This was done in order to have the vortex core in the visualization plane for as long as possible. Fluorescent dye was placed along the edge of the stationary plate before the wall was set in motion.

The instability waves initially appear on the outer turn of the vortex and are ingested into the vortex core. Figure 17 shows the development of the instability waves as Re_Γ increases for a given wall speed. The spanwise length shown in the photographs is 0.16 of the total belt width. It can be seen that the wavelength of the instability remains fixed while the amplitude grows. A movie of this process is available with the online version of the paper (movie 2). The nonlinear growth of these waves eventually results in the breakdown of the primary core. Significant care had to be taken during the execution of experiments as the instability growth rate and wavelength are sensitive to background disturbances. Once the structures have formed, the wavelength does not vary as time increases. No wavelength doubling was observed. Once a wavelength has been established it dominates the flow.

As the wall speed is increased, the instability wavelength becomes shorter. Figure 18 shows instability waves at $Re_\Gamma = 12 \times 10^3$ for three different wall speeds. The presence of mushroom structures on the outer turn of the vortex can be clearly seen in figures 18(*b*) and 18(*c*). This would suggest that a significant reorientation of the spanwise vorticity is occurring. In the range of wall speeds from 17 to $30\,\mathrm{mm\,s^{-1}}$ in water, the instability wave was hard to detect as the structure was extremely sensitive to background disturbances. In the range of wall speeds from 35 to $103\,\mathrm{mm\,s^{-1}}$, the wavelength was relatively easy to measure. Images such as those in figure 18 were processed with a discrete Fourier transformation to extract instability wavelength information. The range of wavenumbers was somewhat scattered due to the irregularity of the streakline profile. Figure 19 shows data for the amplified wavelength, normalized with respect to $Re_U = U_w/\nu$ and plotted with respect to Re_U; Re_U represents a

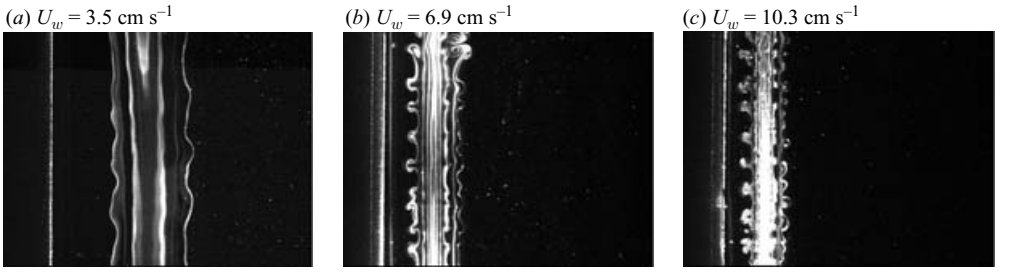

FIGURE 18. Spanwise instability at $Re_\Gamma = 12 \times 10^3$ for wall speeds (*a*) 35 mm s^{-1} (*b*) 69.5 mm s^{-1} and (*c*) 103 mm s^{-1}.

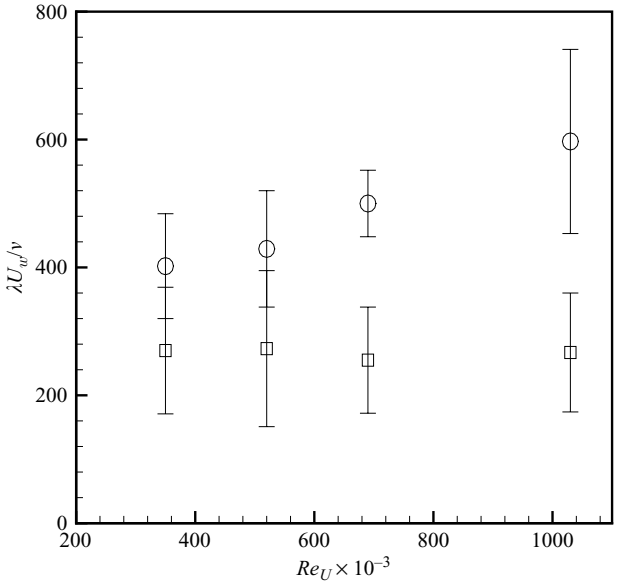

FIGURE 19. Non-dimensional wavelength of the spanwise instability plotted with respect to Re_U : ○, flow visualization; □, PIV data.

unit Reynolds number. The flow visualization data, seen as circles, show a relative insensitivity to Re_U. The error bars indicate the scatter in the range of wavelengths for experiments with a given wall speed. The trend of a reduction in wavelength with increasing wall speed was also observed in the study of Vogel *et al.* (2003).

4.2. *Instability strength*

To determine the strength of these instability structures, PIV measurements were performed in a plane parallel with the axis of the primary core. Figure 20(*a*) shows a visualization image of the vortical structure on the outer turn of the primary vortex. Figures 20(*b*) and 20(*c*) show the corresponding velocity and vorticity fields. The vorticity Ω has been normalized with U_w^2/ν. The peak strength of the instability is of the same order as the peak-vorticity measurements in figure 10. This would indicate that a significant reorientation and stretching of the vorticity has occurred on the separating vortex sheet.

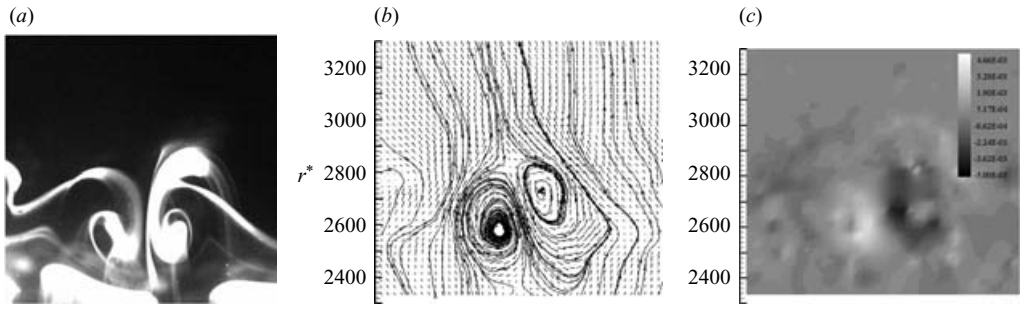

FIGURE 20. Görtler vortex: (*a*) visualization, (*b*) velocity field and (*c*) vorticity distribution.

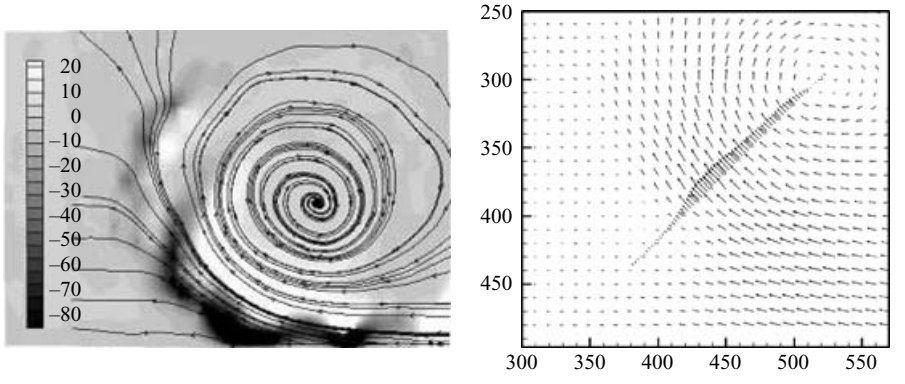

FIGURE 21. (*a*) Rayleigh quotient evaluated from PIV data and (*b*) a cross-section of the two-dimensional velocity field.

4.3. *Instabilty mechanism*

As mentioned in the introduction, this type of flow has topology and boundary-condition similarities with cavity flows; hence it would seem logical to look to the stability of cavity flows for elucidation of a mechanism for the instability observed in the current experiments. Instability discussion in relation to cavity flows has typically revolved around the role of the downstream secondary eddy rather than the effect of the corner singularity. From the flow-visualization experiments it appears that the instability has its source in the region of high shear on the outer turn of the primary vortex. The Rayleigh criteria for the stability of inviscid flows can be used to indicate whether a flow is potentially unstable. Figure 21(*a*) shows the Rayleigh quotient, $\Phi = \mathrm{d}(rV_\theta)/\mathrm{d}r$, evaluated from an instantaneous velocity field; the origin of cylindrical coordinates was set at the vortex core. Potential instability of the flow corresponds to $\Phi < 1$, the region of high shear where the vortex separates from the stationary surface.

Figure 21(*b*) shows a sample PIV data field. Overlaid on this plot is a high-resolution velocity profile in the separating region. This profile resembles a wall jet subject to concave curvature. Such a wall jet is potentially unstable owing to the presence of centrifugal forces (Floryan & Saric 1984). The inner flow, the section of the flow between the wall and the point of maximum velocity, is where the instability will first develop. The instability control parameter for this type of flow is the Görtler

number, $G_o = U_\infty(\delta/\nu)\sqrt{\delta/R}$, where U_∞ is the maximum velocity of the wall jet, R is the radius of curvature and δ is the wall-jet thickness. The criterion for the development of Görtler vortices in the concave wall jet is when $G_o > 1$. There is no critical wavenumber and the characteristics of the instability vortices are determined by the disturbance growth process. The wavelength that develops is the one which has the most amplified rate of growth. Experiments to determine the natural wavelength of Görtler vortices have been found to be extremely sensitive to the properties of the apparatus and its flow field. Bippes (1978) recorded that the wavelength of the Görtler cells in experiments corresponds to those which have the highest amplification rates from linear theory. Once the wavelength is established it is preserved during downstream development of the cells. To support the argument that the instability observed in the current experiments is Taylor–Görtler, an attempt was made to compare the flow-visualization wavelength with theoretical predictions. Floryan (1986) argued that the most amplified wavelength changes with Görtler number and is a function of a dimensionless wavelength parameter Λ defined as $\Lambda = F^{1/3}\lambda^{1/3}\nu^{-1}(\lambda/R)^{1/2}$; F is the dimensional flux of the external momentum; (see Glauert 1956), λ is the dimensional wavelength, ν is the kinematic viscosity and R is the radius of the wall curvature. Floryan (1986) showed that the values of Λ for maximum amplification rate are in the range 48–85 when the Görtler number varies from 5 to 20. While this does not provide a critical wavelength or Görtler number, it does bound the possible instability wavelengths. In the current experiments if we assume a 'quasi-steady' flow, in that we assume that the rate of growth of the instability is considerably faster than the rate of growth of the vortex, $F = \int_0^\infty u(\int_0^\infty u^2\,\mathrm{d}y)\,\mathrm{d}y$ can be approximated from the two-dimensional PIV velocity field. Making an estimate of R and δ from the velocity-field data, estimates can then be made for the instantaneous Görtler number and the associated non-dimensional wavelength that has the most rapid growth rate. Using our estimates for F and R, an estimate of the physical wavelength λ of the instability can be made. Results of this analysis are shown, denoted by squares, in figure 19. Although this analysis is coarse and relies on a quasi-steady assumption, the wavelengths observed in flow-visualization experiments and the predictions from PIV data using this technique are of the same order and show similar trends; hence it is reasonable to conclude that the mechanism for the instability of the junction vortex is Görtler, owing to the presence of centrifugal forces.

5. Conclusions

Experiments have shown that for $Re_\Gamma > 10^3$ a vortex forms close to the junction where a moving wall meets a stationary wall. The data reveals that while the vortical structure is small in relation to the fixed-apparatus length scale, the size and velocity field of the vortex appear to scale in a self-similar fashion. The rate of growth is related directly to the impulse that the moving wall applies to the flow, which results in a prediction that the structure should grow as $t^{5/6}$. This prediction is in good agreement with the experimental results. Self-similar scaling has also been used to collapse the PIV data and produce a universal velocity field for high-Reynolds-number flows. The self-similar entrainment diagram for this high-Reynolds-number flow was determined via the use of isoclines. This technique produces a pattern that consists of a focus, a node at the junction singularity and a saddle close to the stationary plate surface. It is suggested the the mechanism for vortex formation is that the flow passes though a number of low-Reynolds-number states, similar to that of a viscous jet, before attaining the final high-Reynolds-number form in the current experiments.

The three-dimensional spanwise instability that forms on the outer turn of this structure has been quantified with flow visualization and PIV. The instability was found to be extremely sensitive to disturbances and the wavelength of the instability scales inversely with wall velocity. Using experimental PIV data fields to make an estimate of the most unstable modes, based on linear stability, results in a reasonable correlation with the flow visualization results for the spanwise instability. The instability is centrifugal and the nonlinear growth of these structures results in the eventual turbulent breakdown of the structure.

The authors would like to thank Professor Smits at Princeton University and to acknowledge support from NSF-CTS grant number 9706902.

REFERENCES

Aidun, C. K., Triantafillopoulos, N. G. & Benson, J. D. 1991 Global stability of a lid driven cavity with throughflow:Flow visualization studies. *Phys. Fluids* **3**, 2018.

Albensoeder, S., Kuhlmann, H. C. & Rath, H. J. 2001 Three-dimensional centrifugal-flow instabilities in the lid-driven-cavity problem. *Phys. Fluids* **13**, 121–135.

Albensoeder, S. & Kuhlmann, H. C. 2002 Linear stability of rectangular cavity flows driven by anti-parallel motion of two facing walls. *J. Fluid Mech.* **458**, 153–180.

Allen, J. J. & Auvity, B. 2002 Interaction of a vortex ring with a piston vortex. *J. Fluid Mech.* **465**, 453–378.

Allen, J. J. & Chong, M. S. 2000 Vortex formation in front of a piston moving through a cylinder. *J. Fluid Mech.* **416**, 1–28.

Allen, J. J. & Smits, A. J. 2001 Energy harvesting eel. *J. Fluids Struct.* **15**, 629–640.

Bajura, R. A. & Catalano, M. R. 1975 Transition in a two-dimensional plane wall jet. *J. Fluid Mech.* **70**, 773–799.

Bippes, H. 1978 Experimental study of the Laminar-Turbulent transition on a concave wall in a parallel flow. *Tech. Rep. NASA TM* 75243.

Blackburn, H. M. & Lopez, J. M. 2003 The onset of three-dimensional standing and modulated travelling waves in a periodically driven cavity flow. *J. Fluid Mech.* **497**, 289–317.

Cantwell, B. J. 1986 Viscous starting jets *J. Fluid Mech.* **173**, 159–189.

Cantwell, B., Coles, D. & Dimotakis, P. 1978 Structure and entrainment in the plane of symmetry of a turbulent spot. *J. Fluid Mech.* **87**, 641–672.

Conlon, B. P. & Lichter, S. 1995 Dipole formation in the transient planar wall jet. *Phys. Fluids* **7**, 999–1014.

Floryan, J. M. 1986 Görtler Instability of boundary layers over concave and convex walls. *Phys. Fluids* **29**, 2380–2387.

Floryan, J. M. & Saric, W. S. 1984 Wavelength selection of Görtler vortices. *AIAA J.* **22**, 11, 1529–1538.

Glauert, M. B. 1956 The wall jet. *J. Fluid Mech.* **1**, 625–643.

Glezer, A. & Coles, D. 1990 An experimental strudy of a turbulent vortex ring. *J. Fluid Mech.* **211**, 243–283.

Guezet, J. & Kageyama, T. 1997 Aerodynamic study in a rapid compression machine. *Revue Generale de Thermique* **36**(1), 17–25. Elsevier.

Hancock, C., Lewis, E. & Moffatt, H. K. 1981 Effects of inertia in forved corner flows. *J. Fluid Mech.* **112**, 315–327.

Hughes, M. D. & Gerrard, J. H. 1971 The stability of unsteady axisymetric incompressible pipe flow close to a pison. Part 2. Experimental investigation and comparison with computation. *J. Fluid Mech.* **50**, 645–655.

Koseff, J. R. & Street, R. L. 1984*a* Visualization studies of a shear driven three-dimensional recirculating flow. *Trans. ASME: J. Fluids Engng* **106**, 21.

Koseff, J. R. & Street, R. L. 1984*b* The lid-driven cavity flow: A synthesis of qualitative and quantitative observations. *Trans. ASME: J. Fluids Engng* **106**, 391.

Obokata, T. & Okajima, A. 1992 Roll-up vortex on the reciprocating piston in a cylinder. *Sixth Intl Symp. On flow Visualization* (ed. Y. Tanida & H. Miyashiro), pp. 594–598. Springer.

Pan, F. & Acrivos, A. 1967 Steady flow in rectangular cavities. *J. Fluid Mech.* **28**, 643–655.

Stern, M. E. & Pratt, L. J. 1985 Dynamics of vorticity fronts. *J. Fluid Mech.* **161**, 513–532.

Tabaczynski, R. J., Hoult, D. P. & Keck, J. C. 1970 High Reynolds number flow in a moving corner. *J. Fluid Mech.* **42**, 249–255.

Taylor, G. I. 1960 *Aeronautics and Aeromechanics*. Pergamon.

Vogel, M. J., Hirsa, A. H & Lopez, J. M. 2003 Spatio-temporal dynamics of a periodically driven cavity flow. *J. Fluid Mech.* **478**, 197–226.